Chapter 5

Biomedical Applications for Correlation Diffusion

5.1 Blood Flow Monitoring

Near-infrared spectroscopy (NIRS) has long been used to non-invasively measure pulse rate [8, 9, 10] and blood oxygenation [5, 6, 7, 10] and recently to measure blood flow [19, 121]. The advantage of NIRS over laser Doppler blood flowmetry (LDBF) to measure blood flow is that flow in larger volumes of tissue can be monitored. LDBF can only be used to interrogate mm^3 volumes of tissue whereas NIRS can interrogate 1 to 10 cm^3 volumes of tissue. LDBF is restricted to small volumes because quantitative information on blood flow is only available if detected photons have scattered from moving blood cells no more than once. LDBF can be used to quantify blood flow in larger volumes if the blood volume fraction (P_{blood} see eq. (4.53)) is known, however the signal-to-noise is generally prohibitively low for optode separations of 5 mm or larger. The signal-to-noise is limited by the maximum allowed tissue exposure to laser light. ANSI sets this maximum at 0.4 W cm^{-2} at 850 nm for exposures between 10 and 30,000 seconds [122]. NIRS is not restricted in this way since large aperature detectors can be used to collect more diffuse light. However, NIRS methods do make certain assumptions about metabolic activity during blood flow measurements.

After briefly reviewing the NIRS and LDBF methods for measuring blood flow and discussing their shortcomings, I demonstrate the use of correlation diffusion equation as a new tool for quantifying blood flow. This approach is only applicable in the

regime where there have been multiple scattering events from moving particles. As in the case of LDBF, the volume fraction of blood (i.e. P_{blood}) must be known and the signal-to-noise is prohibitively low for optode separations $\geq$5 mm. The advantage of using correlation diffusion analysis over LDBF is that blood flow variations on macroscopic (i.e. $\geq$1 mm) length scales can be quantitatively modeled. In this section I demonstrate the similarity of correlation diffusion to LDBF and in the next section I address the modeling of spatially varying flow.

The concept behind using light to monitor the pulse rate is quite simple. For red light (700-900 nm), the dominate absorber in the body is blood. During a heart beat, the local blood volume increases in the vascular system thus increasing the light absorption. By monitoring fluctuations in the intensity of light that diffuses through the tissue, one is effectively measuring the pulse rate.

Optical measurements of blood oxygen saturation is more sophisticated and relies on spectroscopic differences between oxy- and deoxy- hemoglobin. The absorption spectrum of $\sim$4% hemoglobin is shown in fig. 5.1. Because of the isosbestic point at 800 nm it is possible to measure blood volume independent of oxygenation. The oxygenation is determined by differencing absorption measurements above and below 800 nm [12, 20]. For instance, the absorption coefficients at 780 nm (μ_a^{780}) and 850 nm (μ_a^{850}) are

$$\mu_a^{780} = \varepsilon_{\mathrm{Hb}}^{780}[\mathrm{Hb}] + \varepsilon_{\mathrm{HbO_2}}^{780}[\mathrm{Hb0_2}] \ , \tag{5.1}$$

$$\mu_a^{850} = \varepsilon_{\mathrm{Hb}}^{850}[\mathrm{Hb}] + \varepsilon_{\mathrm{HbO_2}}^{850}[\mathrm{Hb0_2}] \ , \tag{5.2}$$

where $\varepsilon_{\mathrm{Hb}}^{780}$ is the extinction coefficient of deoxy-hemoglobin at 780 nm, $\varepsilon_{\mathrm{HbO_2}}^{780}$ is the extinction coefficient of oxy-hemoglobin at 780 nm, etc. The concentrations of deoxy- and oxy-hemoglobin are respectively [Hb] and [$\mathrm{HbO_2}$]. The oxygen saturation is given by

$$Y = \frac{[\mathrm{HbO_2}]}{[\mathrm{Hb}] + [\mathrm{HbO_2}]} \ . \tag{5.3}$$

Solving eq. (5.1) and eq. (5.2) for [Hb] and [$\mathrm{HbO_2}$] we find that the oxygen saturation

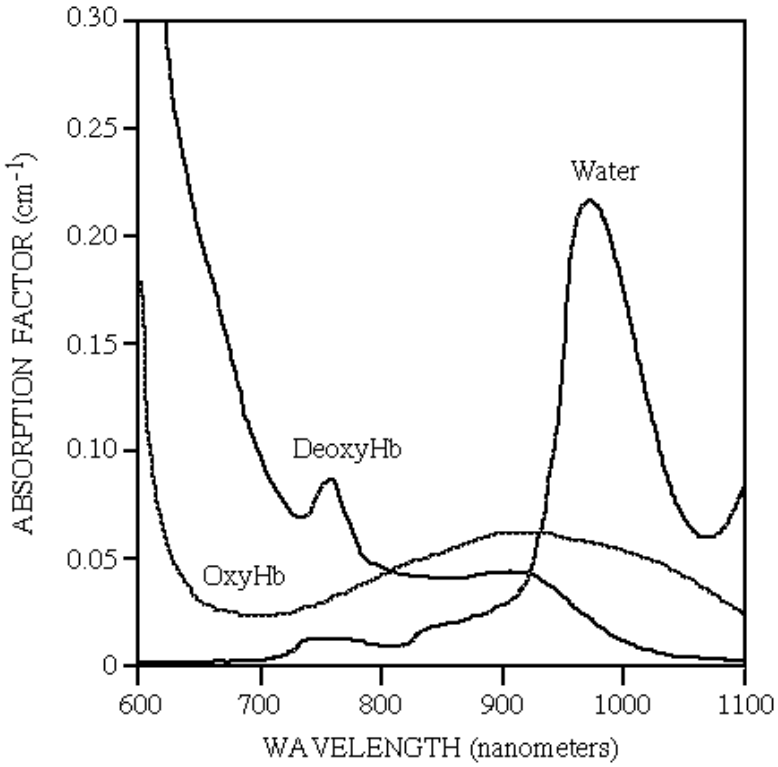

Figure 5.1: The absorption spectra of oxy- and deoxy- hemoglobin are given with that of water. The hemoglobin spectra are given for ∼4% whole blood. The comparison with water absorption indicates the dominance of hemo-globin absorption in the near-infrared and water absorption in the infrared. Absorption due to other biologically relevant chromophores contributes less than 10% of that of hemoglobin and water in the displayed wavelength range.

of hemoglobin can be related to μ_a^{780} and μ_a^{850}, i.e.

$$Y = \frac{\mu_a^{850}\varepsilon_{\mathrm{Hb}}^{780} - \mu_a^{780}\varepsilon_{\mathrm{Hb}}^{850}}{\mu_a^{780}\varepsilon_{\Delta\mathrm{Hb}}^{850} - \mu_a^{850}\varepsilon_{\Delta\mathrm{Hb}}^{780}} \ , \tag{5.4}$$

where $\varepsilon_{\Delta\mathrm{Hb}} = \varepsilon_{\mathrm{HbO_2}} - \varepsilon_{\mathrm{Hb}}$. This method for determining blood oxygen saturation is valid when oxy- and deoxy-hemoglobin are the dominant absorbers. If the absorption by other chromophores is important then the concentration of those other chromophores must also be considered.

NIRS measurements of blood flow derive from Fick's principle and use changes in oxyhemoglobin concentration as an intravascular tracer [19, 121]. Fick's principle states that the rate of accumulation of a tracer is equal to the difference in the rate of arrival and rate of departure of the tracer. If the tracer is oxyhemoglobin then Fick's principle is

$$\frac{\partial}{\partial t}[\mathrm{HbO_2}] = F_{\mathrm{Hb}}\left[[\mathrm{HbO_2}]_+ - [\mathrm{HbO_2}]_-\right] \ , \tag{5.5}$$

where $[\mathrm{HbO_2}]$ is the concentration of oxyhemoglobin, F_{Hb} is the flow of hemoglobin in units of per second, $[\mathrm{HbO_2}]_+$ is the concentration of oxy-hemoglobin arriving, and $[\mathrm{HbO_2}]_-$ is the concentration departing. If a sudden change in the arterial oxygen saturation occurs, the measurement is made before oxygenation change is observed in the venous efflux (i.e. $[\mathrm{HbO_2}]_- = 0$), and during the course of the measurement there is no change in flow, then the hemoglobin flow can be found from

$$F_{\mathrm{Hb}} = \frac{\Delta\mathrm{SaO_2}(t)}{\int_0^t \left(\Delta\mathrm{SaO_2}(t')\right)\mathrm{d}t'} \ . \tag{5.6}$$

$\Delta\mathrm{SaO_2}(t)$ is the total change in arterial blood oxygenation saturation at time t relative to a baseline measurement at $t = 0$ before the oxygen tracer is introduced. This quantity can be measured continuously using NIRS, assuming the venous oxygenation is constant. Sudden changes in arterial oxygenation can be induced by changing the oxygen-nitrogen mixture delivered to the subject through a ventilator, and thus eq. (5.6) suggests a straightforward method to measure arterial blood flow using NIRS.

This method has been used to measure arterial blood flow in the forearm [19] and in the brain [121]. The accuracy of the method has been checked by simultaneous

plethysmographic measurements [19]. Plethysmography is the determination of blood flow by measuring the volume increase in an organ during venous occlusion. This NIR method has been fairly successful in well-controlled situations. With the development of diffusing wave optical tomography [13] it may even permit tomographic imaging of flow.

However, the method does have shortcomings which prevent general applicability. First, this approach requires the subject to control his/her respiration either voluntarily or involuntarily through a respirator so that the oxy-hemoglobin tracer can be introduced. Second, the metabolic activity must be stable so that measured oxygen saturation changes can be ascribed to tracer accumulation. These two restrictions limit the conditions under which blood flow can be measured. Although generally ideal for bed-side monitoring, flow cannot be measured during subject activity (such as exercise) which may be required for the diagnosis of different vascular-related diseases. Furthermore, questions have been raised as to whether blood flow is perturbed by the varying blood oxygenation. Finally, independent measurements of flow and oxygenation cannot be correlated to obtain additional physiological information because of the required control of the oxygenation.

Laser Doppler blood flowmetry provides a different approach with different limitations. In laser Doppler blood flowmetry the Doppler shift of light that has scattered from moving particles is used to derive information about blood flow. This method does not place any restrictions on the subject. Therefore measurements can be made under any conditions. With LDBF, laser light is directed to the tissue, through which it scatters, ocassionally scattering from a moving red blood cell. It then exits the tissue and is detected by a photo-detector. The beating of Doppler-shifted photons with other shifted and unshifted photons results in a fluctuating intensity at the detector. The power spectrum or temporal autocorrelation function of these fluctuations can be used to determine the flow.

The tissue matrix is static relative to the red blood cells and thus does not significantly contribute to any Doppler shift of the light frequency. The blood volume fraction

is generally smaller than 5% (excluding muscles, liver, and other highly perfused organs which can have a blood volume fraction of up to 20%). Thus photons experience Doppler-shifting events infrequently. If the optode separation is small (<2 mm) then detected photons have generally been Doppler-shifted no more than once. LDBF is thus similar to quasi-elastic light scattering except that the scattering angle of the Doppler scattering event is not known. Since more than 10^6 Doppler shifted photons are generally detected per second, the scattering angle is effectively an average over the differential cross section.

The major shortcoming of LDBF is the poor signal-to-noise ratio for optode separation greater than 5 mm. Once again, the signal-to-noise ratio is limited by the maximum laser exposure that tissue can endure. The lack of signal prevents the non-invasive determination of flow in deep tissues. Another disadvantage of LDBF is that the blood volume fraction (i.e. P_{blood}) must be known in order to quantify flow if multiple scattering events have occurred.

The correlation diffusion equation is the multiple scattering limit of LDBF except that the correlation diffusion equation provides a simple framework for considering systems with spatially varying flow and optical properties. To demonstrate the similarity of diffusing temporal correlation spectroscopy and LDBF, I used it to monitor blood flow in the arm during cuff ischemia. Cuff ischemia refers to the use of a pressure cuff to occlude blood flow in a limb thus preventing the delivery of oxygen to the limb. The measurements clearly show blood flow changes with cuff pressures, including the hyperemic overshoot after cuff release. The blood flow measurements are also correlated with changes in blood volume and blood oxygen saturation that were measured using NIRS. The NIRS and correlation measurements were obtained simultaneously.

The experimental system is diagrammed in fig. 5.2. A Ti:Sapphire laser was used to produce CW 800 nm light. The beam was coupled into a 200 μm multimode fiber (NA=0.16) and delivered to the subject's arm. Remission of the light was collected from the sample by a single-mode fiber in order to observe the intensity fluctuations

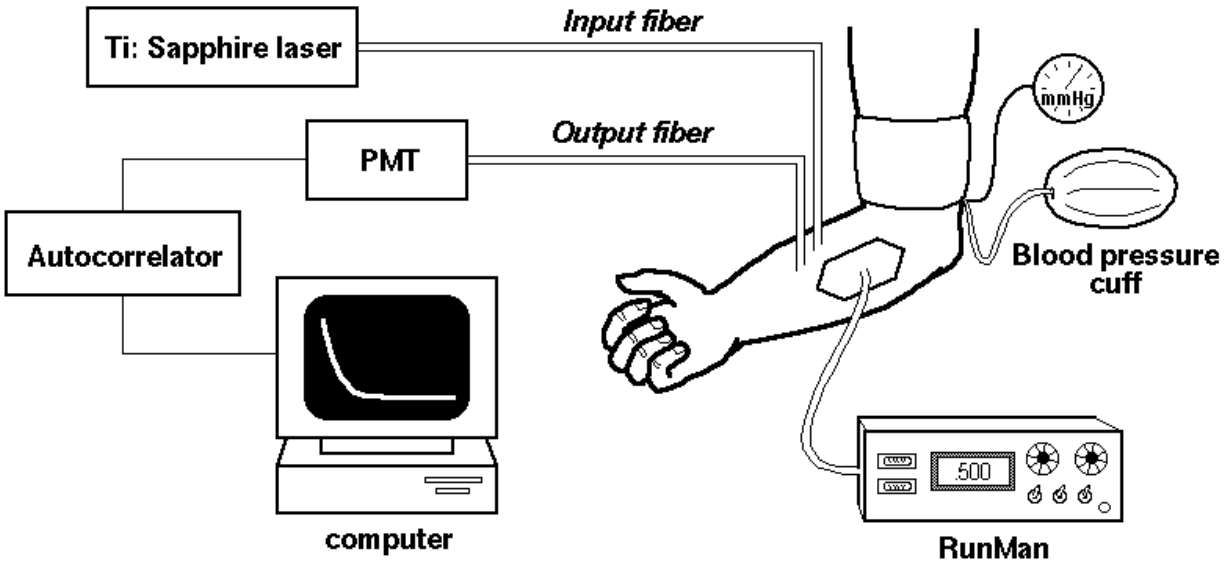

Figure 5.2: Setup for cuff ischemia experiments.

of a single speckle (or mode). The collected light is delivered to a photon-counting photo-multiplier tube (PMT), and the PMT signal is delivered to a digital temporal autocorrelator. Blood volume and oxygenation was measured using a Runman device (NIM Inc., Philadelphia, PA) to measure photon absorption at 760 nm and 850 nm [123]. Each correlation measurement was integrated for 3 minutes while blood volume and oxygenation measurements were gathered continuously. A baseline was measured for the first 18 minutes. The pressure was then quickly raised to 230 mm Hg to simultaneously occlude venous and arterial flow. The response was measured for 12 minutes. The pressure was then released in intervals over the next 15 minutes and measurements made until the flow, volume, and oxygenation returned to normal. These measurements are given in fig. 5.4.

Correlation functions measured during different cuff pressures are shown in fig. 5.3. The decay rate of the correlation function decreases as the cuff pressure is increased. There is a small decrease when the cuff pressure is increased to 50 mm Hg, a large decrease when the cuff pressure is increased to 100 mm Hg, and then a small decrease when the cuff pressure is increased to 150 mm Hg. The large change between

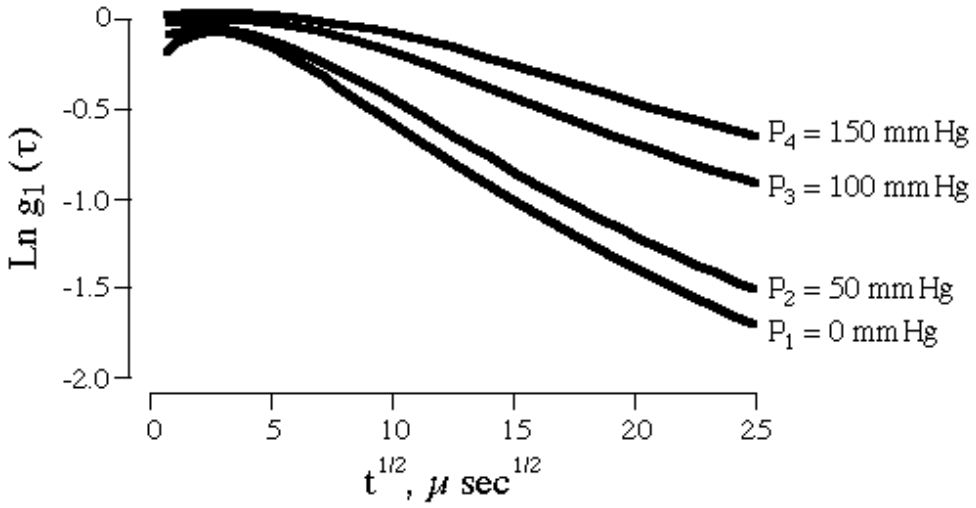

Figure 5.3: The correlation function measured with cuff pressures ranging from 0 mm Hg to 200 mm Hg.

50 mm Hg and 100 mm Hg results from venous occlusion.

During the baseline measurements presented in fig. 5.4, the blood flow, volume, and deoxygenation were found to be constant. During venous and arterial occlusion, the volume did not change but the deoxygenation increased while the flow rapidly decreased. No change in blood volume occurs because blood flow has been abruptly halted, as indicated by the change in flow. The deoxygenation of the blood increases (corresponding to a decrease in oygenation) because of oxygen deliverly to and metabolism by the surrounding cells. When the arteries are opened by dropping the pressure below 150 mm Hg, a significant increase in the blood volume is observed because the arteries are able to deliver more blood to the arm, but at the same time the blood cannot leave because the venous pathways are still occluded. The delivery of fresh blood is also indicated by the drop in blood deoxygenation as well as the increase in blood flow. As the pressure is dropped further the blood volume drops a little because of incomplete venous occlusion allowing blood to leak back to the heart. This notion of leakage is supported by the measured flow increasing as the pressure is decreased. Under normal circumstances the veins remain occluded and the blood volume and flow rate remain fixed until the pressure drops below 80 mm Hg. The observed leakage is

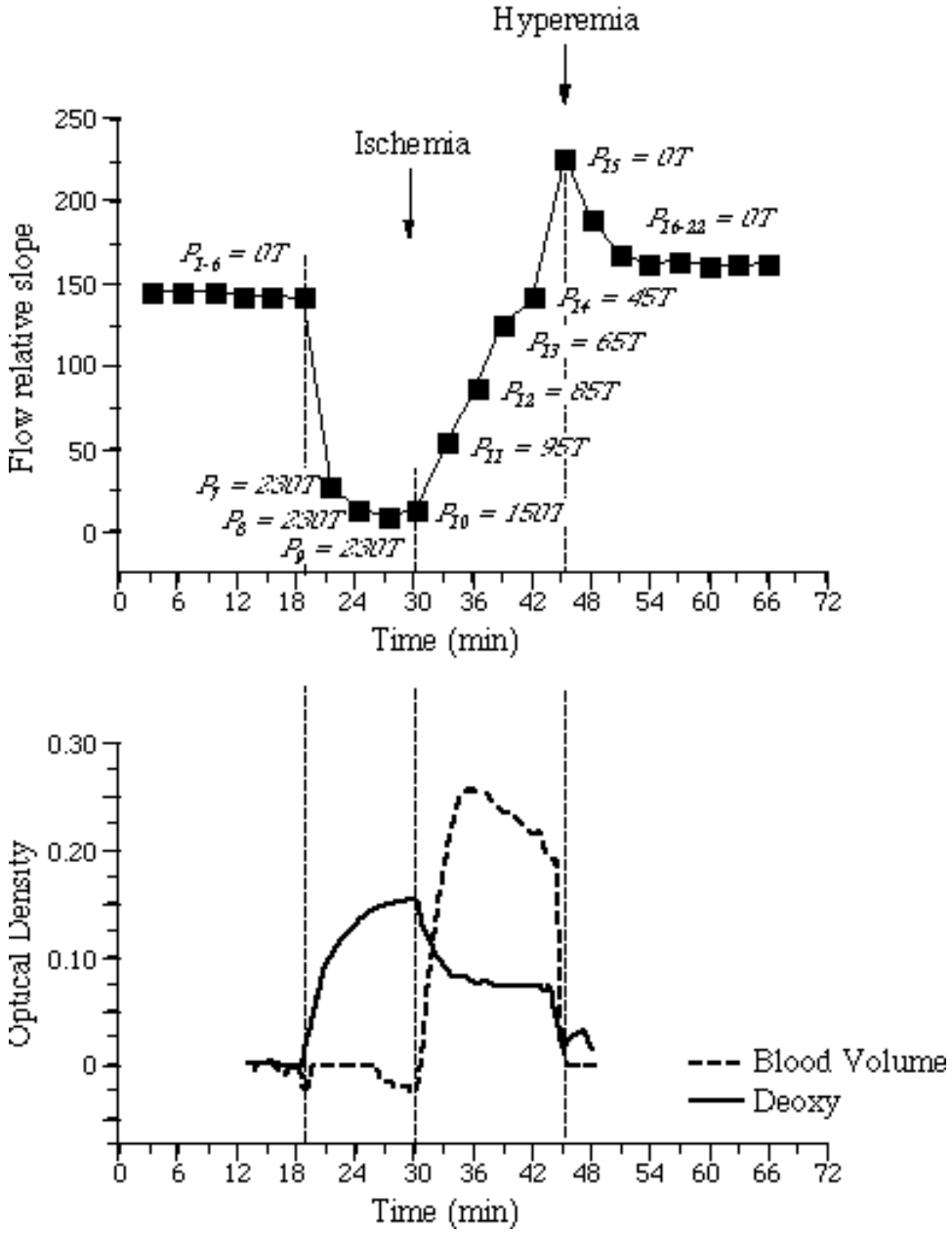

Figure 5.4: The measured decay rate of the correlation function for different cuff pressures applied continuously over an hour is graphed in the top figure. The blood volume and deoxygenation were measured simultaneously and are graphed in the bottom figure.

perhaps a result of our subject's high blood pressure. When the pressure is dropped to zero the blood volume and oxygenation is seen to return to normal but the blood flow first increases above the baseline because of a hyperemic response.

Similar observations have been made using laser Doppler blood flowmetry [124, 125, 126]. In the next section I show how the correlation diffusion spectroscopy can be used to quantify heterogeneous flow.

5.2 Burn Diagnosis

The non-invasive determination of the depth of severe burns has been a tantalizing problem for several years. A robust solution would offer medical practitioners a valuable tool for diagnosing and treating severe burns. Burned tissue is essentially a turbid medium with spatially varying dynamics, i.e. light is multiply scattered by the tissue and layers of burned tissue are characterized by a lack of blood flow, that is, blood flow ceases in severly burned tissue. The dynamical properties of turbid media can be probed by monitoring the temporal fluctuations of the intensities of different speckles emanating from the turbid media. Generally, information on a system's dynamics is obtained from the temporal autocorrelation function of these fluctuations [37, 127, 128]. In chapter 4 I showed that the correlation diffusion equation accurately predicts the temporal correlation function for turbid systems with spatially varying dynamics and that the dynamical properties of such systems can be imaged using reconstruction algorithms based on the correlation diffusion equation [94]. In this section I investigate the sensitivity of temporal field correlation measurements to burn thickness and the applicability of the correlation diffusion equation to absolute determination of burn thickness. Measurements on burn phantoms indicate that 100 μm sensitivity is obtainable and that the correlation diffusion equation predicts the observed correlation function fairly well. These positive results motivated animal studies at the Wellman Institute. Our measurements of various burns on a living pig confirm that 100 μm sensitivity is achievable.

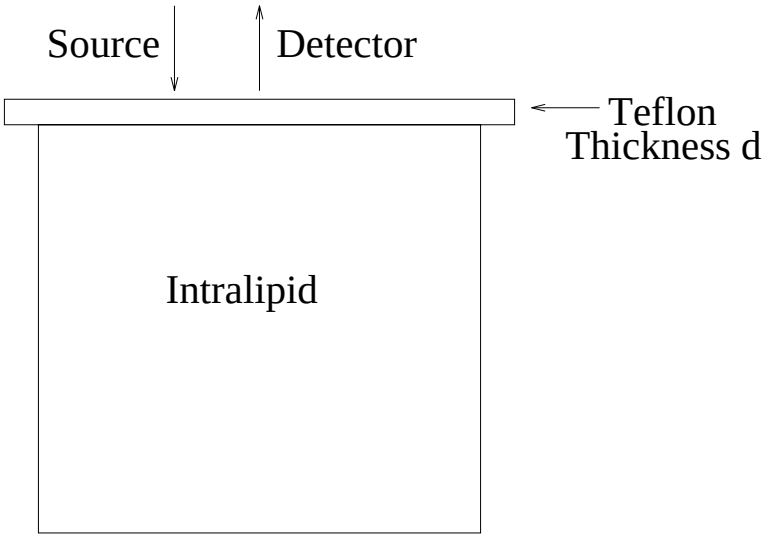

Figure 5.5: Schematic of the burn phantom.

5.2.1 Experiments on Phantoms

The burn phantom is drawn in fig. 5.5. It consists of a layer of teflon resting on a solution of Intralipid. The teflon mimics tissue that has been severely burned in that the teflon scatters light and the scattering particles are static. The Intralipid simulates the scattering and dynamical properties of the healthy tissue underlying the burned tissue. For the teflon μ_s'=79 cm^{-1} and μ_a is negligibly small. A 3.75% solution of Intralipid was used for which μ_s'=55 cm^{-1} and μ_a is negligibly small. For both the teflon and Intralipid solution the absorption was taken to be 0.002 cm^{-1}. The effective Brownian diffusion coefficient of the globules in the Intralipid solution is approximately 10^{-8} cm^{2}s^{-1}, as determined from the mean diameter of 0.4 μm for the globules. Thicknesses of teflon ranging from 0.132 mm to 0.802 mm are used in the experiments to mimic burns of different depths.

The experimental apparatus for probing the dynamical properties of this burn phantom is diagrammed in fig. 5.6. Two different lasers are used, the 514 nm line of an argon ion laser and a helium-neon laser. The laser is coupled into a multi-mode optical fiber (core diameter 200 μm). This fiber delivers the light to the phantom. Several single mode fibers are positioned with the source fiber to collect light at

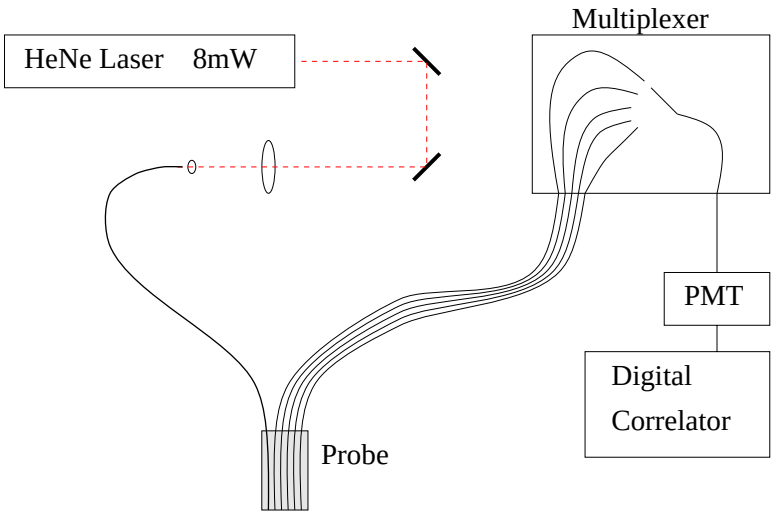

Figure 5.6: Schematic of the experimental setup. Details are given in the text.

distances of 0.2 mm to 2.4 mm from the source. The light collected with the single mode fibers is then delivered to a photon-counting photo-multiplier tube (PMT) and analyzed using a digital temporal autocorrelator. In the experiments presented here, approximately 1 mW of light is incident on the sample and the signal is integrated for 3 minutes. Higher powers are avoided to prevent pulse pile up, i.e. the photon count rate is already at the upper end of the linear response for the PMT. The multi-mode fiber has a numerical aperture of 0.365 and the single mode fibers are designed for 820 nm light. A better signal-to-noise ratio is obtainable by reducing the numerical aperture of the source fiber and using single mode fibers for 514 nm light.

The normalized field correlation function measured for different source-detector separations on the burn phantom with a teflon thickness of 0.65 mm is graphed in fig. 5.7. The decay of the correlation function arises from the dephasing of photons that have traveled different path lengths through the sample. Long path lengths contribute to the decay of the correlation function at short times while short path lengths dominate at long times. For an infinite homogeneous system where the dynamics are governed by Brownian motion, the correlation function decays exponentially as the square-root of the correlation time. This decay would appear as a straight line in fig. 5.7. The

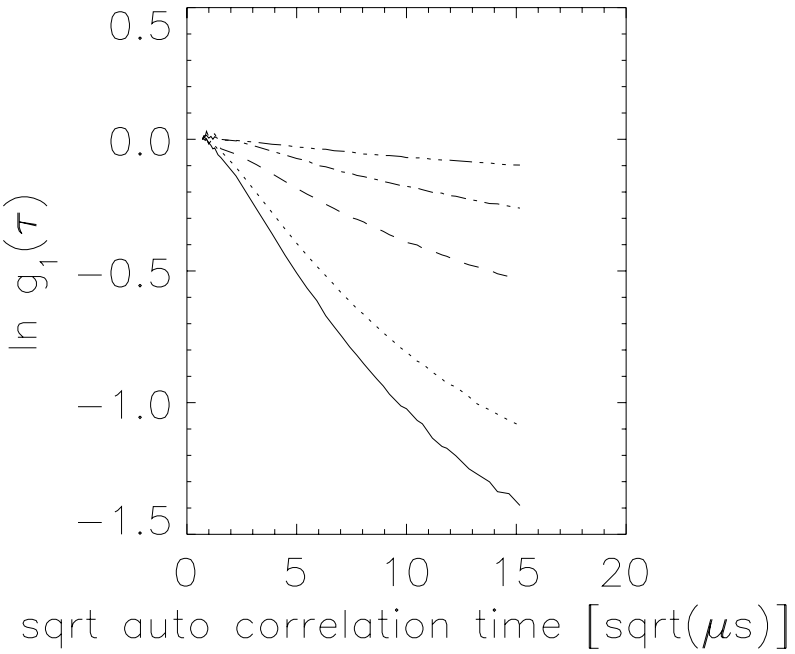

Figure 5.7: The natural log of the normalized field correlation function is plotted versus the square-root of the correlation time for different source-detector separations. The teflon sheet is 0.65 mm. The solid line is for a separation of 2.0 mm and the other lines in order of decreasing slope come from separations of 1.8, 1.2, 0.8, and 0.4 mm.

decay is the same for semi-infinite homogeneous systems except at short times where the decay is inhibited by the loss of long path length photon trajectories. The data presented in fig. 5.7 is nearly linear between 10 and 130 μs. The deviation from linearity at longer times arises from the teflon layer. Specifically, the decay at longer times comes from photons that have traveled short path lengths. In the burn phantom, the short path length photons dwell mostly in the static teflon layer, thus inhibiting the decay of the correlation function.

In addition to the deviation from linearity, the rate of decay in the "linear" region is also perturbed by the presence of the static layer. Fig. 5.8 plots the normalized field temporal correlation function for different teflon thicknesses with a source-detector separation of 1.2 mm. A significant difference is observed in the rates of decay for different teflon thicknesses. Fig. 5.8 indicates that these correlation measurements are sensitive to changes in the teflon thickness smaller than 100 μm.

To summarize the data for all teflon thicknesses and source-detector separations, I plot the slope of the correlation function in the linear region versus source-detector separation for different thicknesses, fig. 5.9a, and versus thickness for different separations, fig. 5.9b. In all cases, the linear region is taken to be between 5 μs and 130 μs.

First consider the slope as a function of source-detector separation for different thicknesses, fig. 5.9a. When no static layer is present, both theory and experiment (not shown) demonstrate that the slope of the correlation function grows linearly with source-detector separation. As seen in fig. 5.9a, the slope *does not* grow lineary with ρ when a static layer of sufficient thickness is present. However when the static layer is sufficiently small (in this case, when d=0.132 mm), the slope is observed to increase linearly with ρ. This observed behavior is expected. Photons in general spend a negligible amount of time in the static layer when its thickness is small. The static layer is thus effectively not there and we observe that the slope increases linearly with ρ. For thicker static layers however, photons spend a significant amount of time in the static layer and thus the correlation function does not decay as rapidly. As the source-

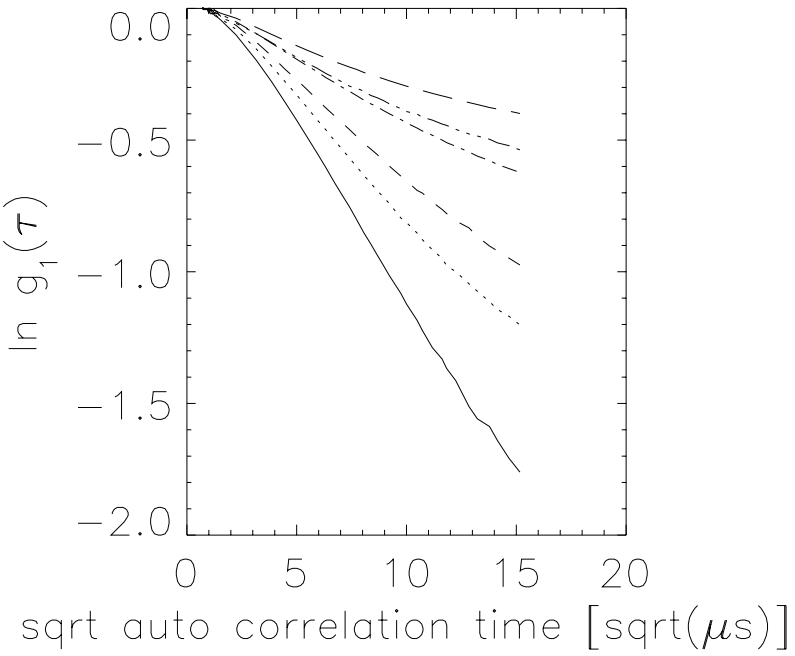

Figure 5.8: The natural log of the normalized field correlation function is plotted versus the square-root of the correlation time for different teflon thicknesses. The source-detector separation was held fixed at 1.2 mm. The solid line is for a thickness of 0.132 mm. The other lines in order of decreasing slope are for thicknesses of 0.258, 0.408, 0.517, 0.650, and 0.802 mm.

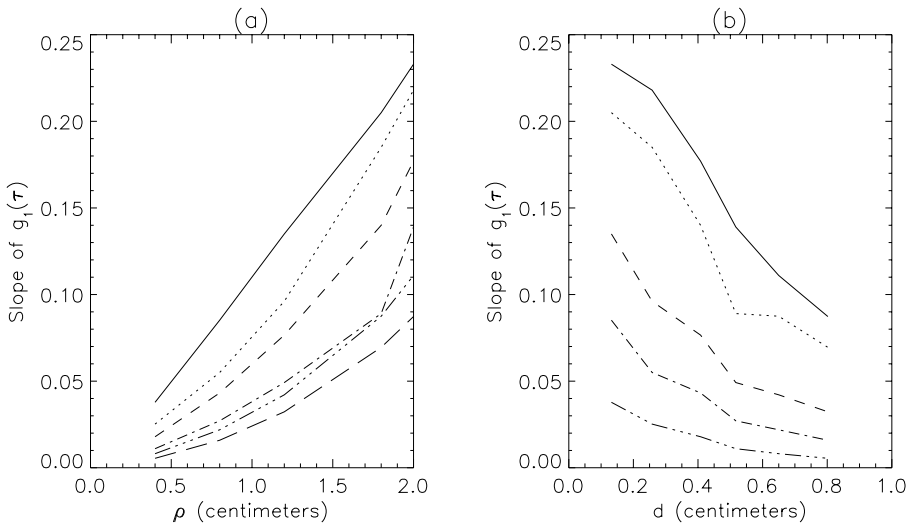

Figure 5.9: Slopes of the experimental data in the nearly linear region between 10 and 130 μs are given versus source-detector separation and teflon thickness. In (a) the slope is plotted versus separation for different thicknesses. The solid line corresponds to a thickness of 0.132 mm, and the other lines moving from the solid line are for thicknesses of 0.258, 0.408, 0.517, 0.650, and 0.802 mm. In (b) the slope is plotted versus teflon thickness for different separations. The solid line corresponds to a separation of 2.0 mm. The other lines, moving from the solid line, are for separations of 1.8, 1.2, 0.8, and 0.4 mm.

detector separation is increased, the photons are spending a smaller percentage of the time in the static layer and thus the slope is seen to increase faster than linear. For larger source-detector separations the slopes are expected to asymptotically approach the value expected for a system with no static layer. This is observed for separations greater than 10 mm when using teflon sheets less than 1 mm thick (not shown).

The slope versus thickness is plotted in fig. 5.9b for different ρ. This graph indicates that the slope decreases rapidly over a short range of thicknesses and that the center of this range depends on the source-detector separation. At smaller thicknesses the slope flattens (as seen for ρ=2.0 mm) because the photons dwell mostly in the dynamical region. The slope also flattens at larger thicknesses (as seen for ρ=0.4, 0.8, and 1.2 mm) since the photons are then spending most of the time in the static region.

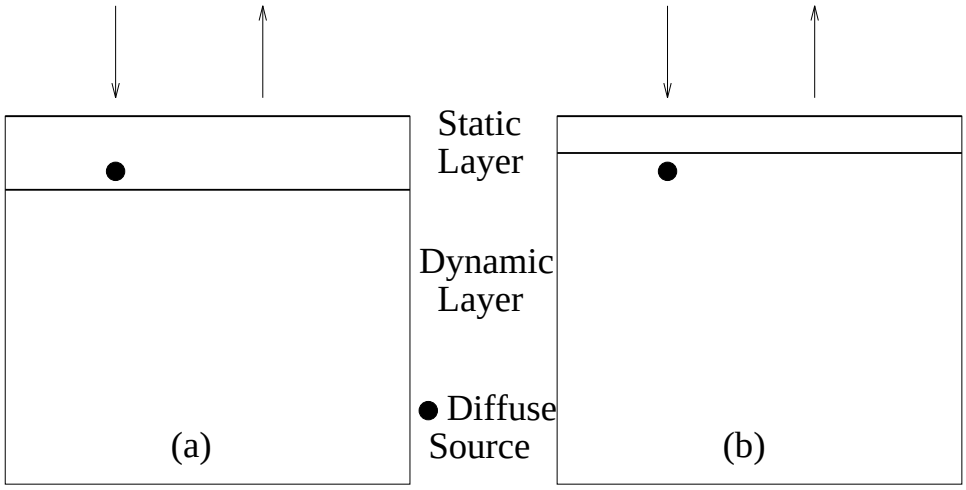

Figure 5.10: (a) and (b) illustrate two possible cases to be considered when obtaining an analytic solution of the diffusion equation for layered media. A collimated source is generally treated as a point diffuse source extended a distance of l^* into the medium. In (a) the thickness of the static layer is greater than l^*. In (b) the thickness of the static layer is smaller than l^*.

The rapid change in the slope occurs when the photons are evenly sampling both regions.

These measurements can be modeled with a solution of the correlation diffusion equation for the system depicted in fig. 5.5. As a reminder the correlation diffusion equation is

$$\Big(- D_\gamma \nabla^2 + v\mu_a + 2\mu_s' v D_B k_o^2 \tau \Big) G_1(\mathbf{r}, \tau) = v S(\mathbf{r}) \; . \tag{5.7}$$

Here $G_1(\mathbf{r}, \tau) = \langle E(\mathbf{r}, t) E^*(\mathbf{r}, t + \tau) \rangle$ is the unnormalized temporal electric field autocorrelation function at the position $\mathbf{r}$ within the sample, $D_\gamma = v/(3\mu_s')$ is the photon diffusion coefficient within the sample, μ_s' is the reduced scattering coefficient, μ_a is the absorption coefficient, and v is the speed of light in the medium. The $\langle \ldots \rangle$ denote an ensemble average or, in the case of an ergodic system, an average over time t. D_B is the particle diffusion coefficent within the medium, k_o is the wavenumber of the light in the medium, and τ is the correlation time. The source light distribution is given by $S(\mathbf{r})$.

To solve the diffusion equation, I approximate the collimated source as an isotropic

point source displaced a distance $z_o = 1/\mu_s'$ into the medium along the axis of the collimated source. I also use the approximate extrapolated-zero boundary condition instead of the exact zero-flux boundary condition (partial flux in the case of an index mismatch). For the extrapolated-zero boundary condition, the field correlation is taken to be zero at $z = z_b = -2/(3\mu_s')$, where the physical boundary is at $z = 0$. The diffusion equation must be solved for two cases: 1) when the point source is in the static layer, and 2) when the point source is displaced into the dynamic region (see fig. 5.10). In the first case, $G_1(\mathbf{r},\tau)$ measured on the surface of the static layer a distance ρ from the source is given by

$$G_1(\mathbf{r},\tau) = \frac{\exp\left(-k_1(\tau)\sqrt{\rho^2+z_o^2}\right)}{4\pi\sqrt{\rho^2+z_o^2}} - \frac{\exp\left(-k_1(\tau)\sqrt{\rho^2+(z_o+2z_b)^2}\right)}{4\pi\sqrt{\rho^2+(z_o+2z_b)^2}} + \int_0^\infty \lambda \mathrm{d}\lambda A(\lambda) J_0(\lambda\rho) \frac{\sin\left(\sqrt{k_1^2(\tau)-\lambda^2}\,(z+z_b)\right)}{\sqrt{k_1^2(\tau)-\lambda^2}} \,. \tag{5.8}$$

Here $k_1^2(\tau) = v^{(1)}\mu_a^{(1)}/D_\gamma^{(1)}$ is the correlation "wavenumber" in the static layer, $J_0(x)$ is a cylindrical Bessel function, and $A(\lambda)$ is a constant that depends on the thickness of the static layer and the properties of the dynamical medium. This constant is

$$A(\lambda) = -\left[\exp\left(iX(\lambda)(d-z_o)\right) - \exp\left(iX(\lambda)(d+2z_b+z_o)\right)\right] \frac{D_\gamma^{(2)}Y(\lambda) - D_\gamma^{(1)}X(\lambda)}{D_\gamma^{(1)}X(\lambda)\cos\left[X(\lambda)(d+z_b)\right] - iD_\gamma^{(2)}Y(\lambda)\sin\left[X(\lambda)(d+z_b)\right]} \,, \tag{5.9}$$

$X(\lambda) = \sqrt{k_1^2(\tau)-\lambda^2}$ and $Y(\lambda) = \sqrt{k_2^2(\tau)-\lambda^2}$ where $k_2(\tau) = \left(v^{(2)}\mu_a^{(2)} + 2v\mu_s'^{(2)}D_B k_o^2\tau\right)/D_\gamma^{(2)}$ is the correlation "wavenumber" in the dynamical medium.

The solution for the second case is

$$G_1(\mathbf{r},\tau) = \int_0^\infty \lambda \mathrm{d}\lambda J_0(\lambda\rho) \frac{-2iD_\gamma^{(2)}\exp\left(iY(\lambda)\,(z_o-d)\right)\,\sin\left(X(\lambda)z_b\right)}{D_\gamma^{(1)}X(\lambda)\cos\left[X(\lambda)\,(d+z_b)\right] - iD_\gamma^{(2)}Y\sin\left[X(\lambda)\,(d+z_b)\right]} \,. \tag{5.10}$$

Comparisons between experiment and diffusion theory are made in fig. 5.11. The parameters used in the calculation are given in the text discussing fig. 5.5. The

agreement between experiment and theory, although not perfect, is pretty good and certainly captures the trend as a function of source-detector separation and static layer thickness. It is interesting to note that the agreement is better at larger thicknesses where the diffusion theory is expected to be more valid in the static layer. The larger disagreement at smaller thicknesses is most likely a result of the breakdown of the diffusion approximation in the small static layer. In this regime, comparison with a solution of the correlation transport equation [57, 58] would be more appropriate.

As seen from figs. 5.9a and b, measurements of the temporal field correlation function are sensitive to variations of less than 100 μm in the teflon thickness. Furthermore, there is a correspondence between the thickness of the "burn" and the slope of the correlation function versus the source-detector separation (see fig. 5.9a). Burn thickness can thus, in principle, be determined from correlation measurements with an accuracy of better than 100 μm. However, an accurate determination depends on the established correspondence which, in general, is a function of the optical and dynamical properties of the burned tissue. It is thus important to investigate, numerically and experimentally, the dependence of the curves in fig. 5.9a on the optical and dynamical properties. For instance, we might find that a ratio of the slope of the correlation function measured on the burn to that measured over healthy tissue is relatively independent of the optical properties.

Fig. 5.9b suggests that these measurements would be suitable in a feedback loop for controlling an automatic laser ablation system. By first choosing a large source-detector separation such that the sensitivity of the slope of the correlation function to the burn depth is optimized, we can observe the preliminary layers of necrotic tissue being removed. As the burn thickness is decreased, smaller and smaller source-detector separations are monitored to maintain optimal sensitivity. For correlation measurements to be effective in a feedback system, a decent signal must be obtainable in a second. The measurements presented here were integrated for 3 minutes to obtain the best signal-to-noise ratio for presentation purposes. In fact, a sufficient signal-to-noise ratio is achieved after only a few seconds for the parameters used in the phantom

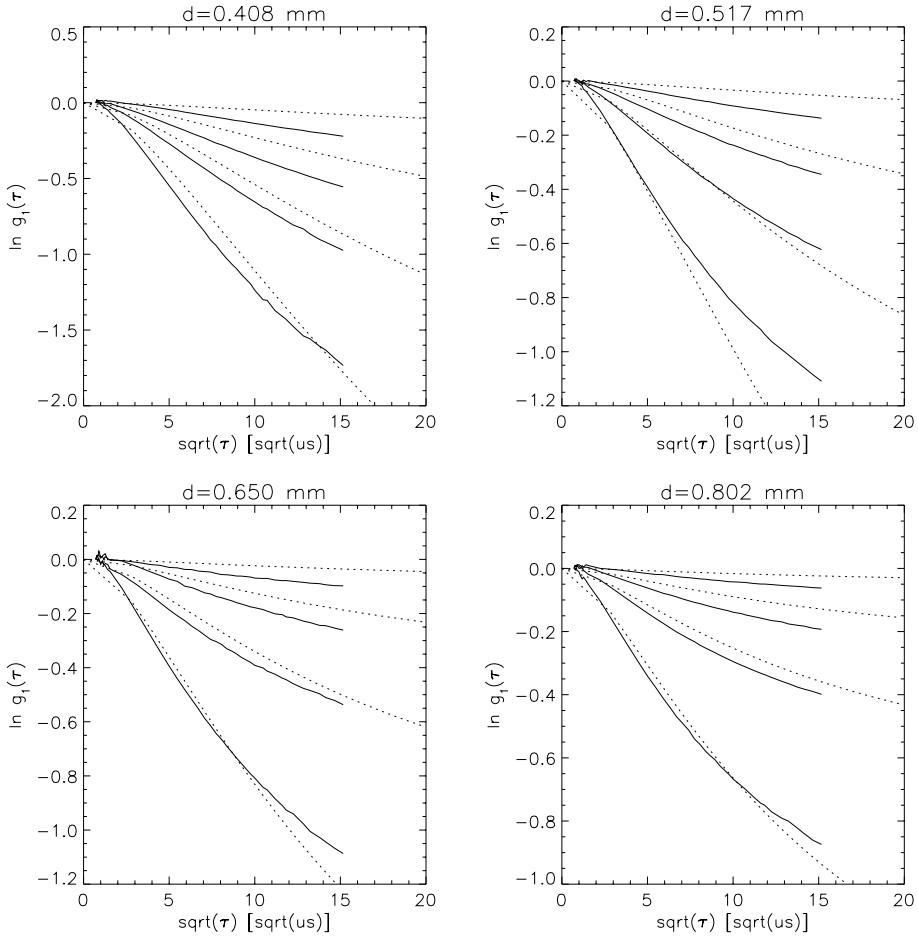

Figure 5.11: Comparisons between the experimental data and that predicted by theory for different thicknesses and separations are given. Each graph shows the results for a particular thickness of teflon. The solid lines are the experimental data and the dotted lines are theoretical. Results for separations of 0.4, 0.8, 1.2, and 1.8 mm are given.

trials. As mentioned, a better signal-to-noise ratio can be achieved by optimizing the fiber optics. In addition, since the photon count rate is so high, analog measurements of the correlation function may be possible. Analog measurements provide a higher duty cycle and thus a better signal-to-noise ratio.

The reduced scattering coefficient of the teflon and Intralipid is approximately 80 cm^{-1} and 50 cm^{-1} respectively. The reduced scattering coefficient for tissue is around 10 cm^{-1}. The absorption of tissue is $\sim$0.05 cm^{-1}. Measurements on tissue may not significantly alter the conclusions, but the accuracy of the correlation diffusion equation on the length scales of interest will be jeopardized because of the smaller reduced scattering coefficient.

The agreement between the correlation diffusion theory and the experimental results is encouraging. This theory will permit measurements of burn thickness to be quantified.

5.2.2 Clinical Work

After verifying with measurements on phantoms that photon correlation techniques are sensitive to differences in thickness of 100 μm and that the correlation diffusion equation (eq. (4.22)) can be used to model the correlation function, my next step was to apply the technique clinically. The clinical work was done with Norm Nishioka and Kevin Schomacker at the Wellman Institute in Boston. We used their pig burn model for the clinical trials [129].

This work was made possible by an Army grant to develop and investigate the efficacy of a laser debridement system. Debridement refers to the removal of dead tissue. Their debridement system is operational and is currently being tested with pigs since the skin of pigs closely resembles that of humans. As part of the Army grant, the Wellman Institute has been investigating possible optical feedback techniques for controlling the debridement. The idea is to use an optical technique to identify severely burned tissue and then provide feedback during the debridement process to determine when the severly burned tissue has been completely removed. Diffuse reflectance

Table 5.1: Burn depths were assessed from biopsied tissue using a LDH stain (lactate dehydrogenase). LDH is a vital stain, therefore it will not stain cells which are deadened by the burn.

Duration of Burn (sec)	Burn Depth (μm)
3	60-100 (epidermal)
5	400-500
7	500-600
12	1500-2000
20	2100-2200

[130, 131], fluorescence indicators of blood flow [132, 133], laser doppler [134, 135], and speckle visibility [136] techniques are being considered for this project.

To probe burn depth, we used the same experimental system that I used in the phantom studies (see fig. 5.12). The pig was anesthetized and stablized on an operating table in an operating suite at the Wellman Institute. Burns were administered using 2 inch square metal blocks brought to 100 °C by boiling water. Burn thickness was controlled by applying the metal block to the skin for a duration of 1 to 20 seconds. For our study, five different burns were examined. The duration and depth of each burn is provided in table 5.1. I measured the correlation function on each burn for source-detector separations ranging from 0.2 mm to 2.4 mm. Measurements were made 48 hours after the administering of the burn.

Prior to burning the tissue, measurements were made at various positions on the skin to determine a baseline. Also, baselines were periodically measured on healthy tissue between measurements of the burned tissue. A set of preburn measurements at a single site is shown in fig. 5.13. Here we see the single exponential decay of the correlation function, and that the decay rate increases linearly with the source-detector

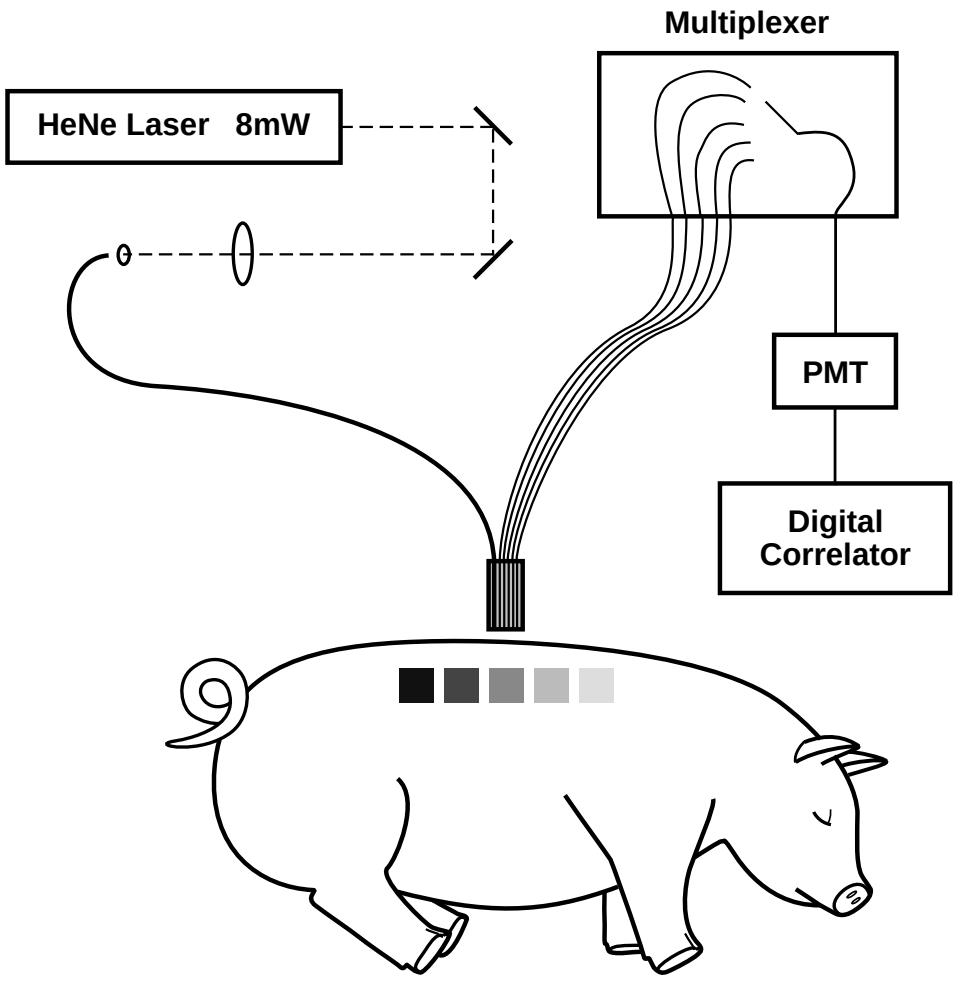

Figure 5.12: Experimental setup for the pig experiments. The shaded areas on the pig indicate burns of various depths.

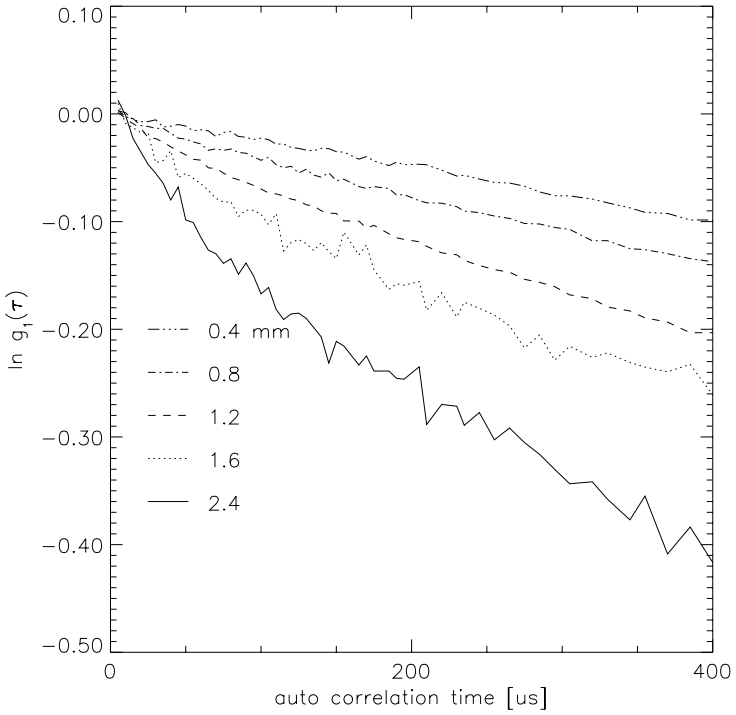

Figure 5.13: Correlation functions at a preburn site for different source-detector separations is presented. The separations are indicated in the legend.

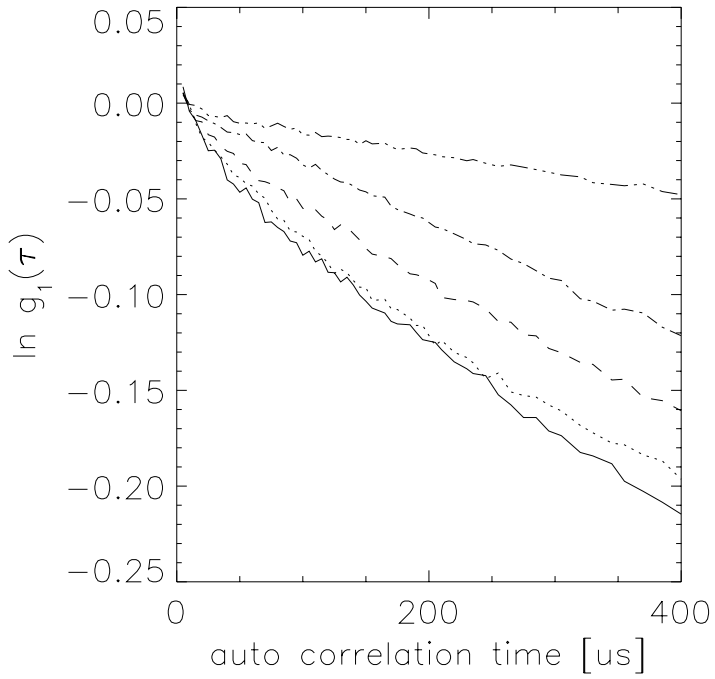

Figure 5.14: The temporal field correlation functions obtained from the 48 hour old burns for a source-detector separation of 800 μm are plotted. The correlation functions for the 3 s (solid line), 5 s (dotted line), 7 s (dashed line), 12 s (dot-dash line), and the 20 s (dot-dot-dot-dash line) burns are presented.

separation.

Fig. 5.14 plots the temporal field correlation functions obtained from the 48 hour old burns for a source-detector separation of 800 μm. As expected, the decay rate of the correlation function decreases as the burn thickness increases. These data indicate that the 5, 7, 12, and 20 second burns are easily distinguished. To summarize the data for all source-detector separations, I determined the decay rate of the correlation function for $0 < \tau < 100$ μs by fitting a line to the data, and plot the decay rate as a function of source-detector separation for different burns. These results are given in fig. 5.15 and indicate that it is possible to distinguish burns that vary in thickness by only 100 μm. The behavior of the decay rate is expected. For shallow burns,

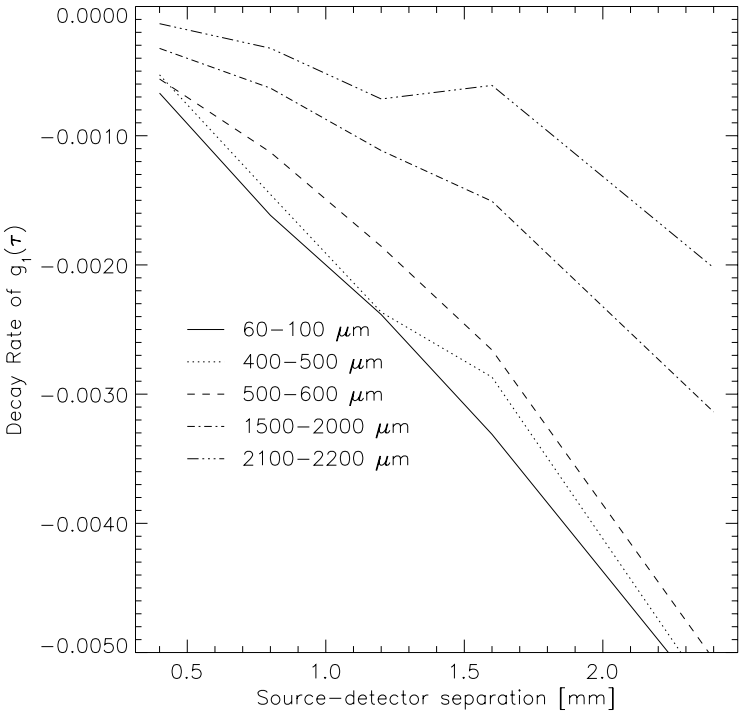

Figure 5.15: The decay rate of the correlation function versus source-detector separation is graphed for different burns. The burn depths are indicated in the legend.

the decay rate increases linearly with the source-detector separation as observed for healthy tissue and expected for a homogeneous system, i.e. the shallow burn does not perturb the correlation function. However, for deeper burns, the decay rate decreases and no longer increases linearly with the source-detector separation.

Our results from this clinical study are encouraging in that they verify that correlation measurements can be used to distinguish burns with thicknesses that vary by 100 μm. More research is needed to quantify the burn thickness from the raw data. The quantification will require knowledge of the optical and dynamical properties of the burn. It should be possible to determine these quantities from the correlation measurements and from diffuse reflectance measurements in the time-domain and/or frequency domain (see chapter 2). This quantification may be simplified by comparing correlation functions between burned and healthy tissue. A ratio of such measurements

may be insensitive to blood flow, thus reducing the number of unknowns in the determination of the burn depth. Finally, the behavior of the burns during the first few hours must be studied more carefully to determine if correlation techniques can be used to diagnose the severity of young burns. To be a suitable diagnostic tool, our technique must be able to characterize burns during the first day, preferably within the first six hours. This research is in progress.